

Numerical simulation on dendritic growth of Al-Cu alloy under convection based on the cellular automaton lattice Boltzmann method

Kang-Wei Wang(王康伟), Meng-Wu Wu(吴孟武), Bing-Hui Tian(田冰辉), and Shou-Mei Xiong(熊守美)
Citation: Chin. Phys. B, 2022, 31 (**9**): 098105. DOI: 10.1088/1674-1056/ac7211
Journal homepage: http://cpb.iphy.ac.cn; http://iopscience.iop.org/cpb

What follows is a list of articles you may be interested in

Multi-phase field simulation of competitive grain growth for directional solidification

Chang-Sheng Zhu(朱昶胜), Zi-Hao Gao(高梓豪), Peng Lei(雷鹏), Li Feng(冯力), and Bo-Rui Zhao(赵博睿)
Chin. Phys. B, 2022, 31 (**6**): 068102. DOI: 10.1088/1674-1056/ac4486

A high-quality-factor ultra-narrowband perfect metamaterial absorber based on monolayer molybdenum disulfide

Liying Jiang(蒋黎英), Yingting Yi(易颖婷), Yijun Tang(唐轶峻), Zhiyou Li(李治友),Zao Yi(易早), Li Liu(刘莉), Xifang Chen(陈喜芳), Ronghua Jian(简荣华),Pinghui Wu(吴平辉), and Peiguang Yan(闫培光)
Chin. Phys. B, 2022, 31 (**3**): 038101. DOI: 10.1088/1674-1056/ac1e11

Numerical study of growth competition between twin grains during directional solidification by using multi-phase field method

Chang-Sheng Zhu(朱昶胜), Ting Wang(汪婷), Li Feng(冯力), Peng Lei(雷鹏), and Fang-Lan Ma(马芳兰)
Chin. Phys. B, 2022, 31 (**2**): 028102. DOI: 10.1088/1674-1056/ac0eed

Phase-field study of spinodal decomposition under effect of grain boundary

Ying-Yuan Deng(邓英远), Can Guo(郭灿), Jin-Cheng Wang(王锦程), Qian Liu(刘倩), Yu-Ping Zhao(赵玉平), and Qing Yang(杨卿)
Chin. Phys. B, 2021, 30 (**8**): 088101. DOI: 10.1088/1674-1056/abea9b

Weakening effect of plastic yielding inception in thin hard coating systems

Xiao Huang(黄啸), Shujun Zhou(周述军), and Tianmin Shao(邵天敏)
Chin. Phys. B, 2021, 30 (**3**): 038104. DOI: 10.1088/1674-1056/abc544

Numerical simulation on dendritic growth of Al–Cu alloy under convection based on the cellular automaton lattice Boltzmann method

Kang-Wei Wang(王康伟)[1,2], Meng-Wu Wu(吴孟武)[1,2,†], Bing-Hui Tian(田冰辉)[1,2], and Shou-Mei Xiong(熊守美)[3]

[1] *School of Automotive Engineering, Wuhan University of Technology, Wuhan* 430070, *China*
[2] *Hubei Key Laboratory of Advanced Technology for Automotive Components, Wuhan University of Technology, Wuhan* 430070, *China*
[3] *School of Materials Science and Engineering, Tsinghua University, Beijing* 100084, *China*

(Received 28 January 2022; revised manuscript received 20 April 2022; accepted manuscript online 23 May 2022)

A numerical model is developed by coupling the cellular automaton (CA) method and the lattice Boltzmann method (LBM) to simulate the dendritic growth of Al–Cu alloy in both two and three dimensions. An improved decentered square algorithm is proposed to overcome the artificial anisotropy induced by the CA cells and to realize simulation of dendritic growth with arbitrary orientations. Based on the established CA-LBM model, effects of forced convection and gravity-driven natural convection on dendritic growth are studied. The simulation results show that the blocking effect of dendrites on melt flow is advanced with a larger number of seeds. The competitive growth of the converging columnar dendrites is determined by the interaction between heat flow and forced convection. Gravity-driven natural convection leads to highly asymmetric growth of equiaxed dendrites. With sinking downwards of the heavy solute, chimney-like or mushroom-like solute plumes are formed in the melt in front of the columnar dendrites when they grow along the gravitational direction. More details on dendritic growth of Al–Cu alloy under convection are revealed by 3D simulations.

Keywords: simulation, cellular automaton, dendritic growth, melt convection

PACS: 81.30.Fb, 47.11.–j, 68.08.De, 81.10.–h **DOI:** 10.1088/1674-1056/ac7211

1. Introduction

Metal solidification is a complex liquid-solid phase transition process accompanied by solute and temperature changes in both the macro and micro scales.[1,2] Those changes cause natural convection in the solidification process of metal alloys. In addition, there is forced convection induced by external force fields such as electromagnetic stirring or ultrasonic vibration during the metal solidification process.[3–5] The melt flow behavior has a great impact on the dendritic growth, which in turn affects the metal alloy solidification structure and the formation of defects such as solute segregation, shrinkage, and porosity.[6] Therefore, an in-depth understanding and mastery of the dendritic growth law under melt convection could help researchers to give suggestions for controlling the microstructure formation and improving the performance of metal alloys.

Owing to the rapid development of x-ray radioscopy technique, *in situ* observation of alloy solidification process becomes possible.[7–12] Shevchenko *et al.*[8,9] directly observed the solute segregation during solidification of Ga–In alloys by x-ray radioscopy and studied the effect of natural and forced convection on dendritic growth. Clarke *et al.*[12] observed the directional solidification of Al–Cu alloys under different temperature gradients by the synchrotron x-ray technique. They found that melt convection increases the stability of the planner interface at a higher growth velocity. Though the dendritic growth process has already been observed realistically and directly through the experimental method, there are still many limitations. Firstly, the applicable alloy system is limited to a small range. Secondly, it is of a great challenge to construct a precise flow field during metal solidification and observe the dendritic evolution in real time. Finally, there are difficulties in distinguishing the effects of various influencing factors on dendritic growth quantitatively.

Over the past few decades, numerical simulation has become an effective method to predict microstructure evolution, such as columnar-to-equiaxed transition,[13–15] dendritic motion,[16,17] and porosity formation.[18] The approaches of microstructure simulation include Monte Carlo,[19] phase field,[20,21] and cellular automaton (CA) methods.[22,23] In particular, the CA method can accurately describe the dendrite morphology under the interaction of heat and solute and has the advantage of high computational efficiency with a large calculation domain. Therefore, it has become the mainstream and hotspot in the field of micro-mesoscopic structure simulation. Combining a CA model with momentum and solute transfer, Zhu *et al.*[24] studied the influence of forced convection on the equiaxed and columnar dendritic morphology of Al–Cu alloy in two dimensions. Subsequently, Sun *et al.*[25] and Yin *et al.*[26] developed a cellular automaton-lattice Boltzmann (CA-LB) model, in which the CA method was used to simulate the dendritic growth and the LBM was applied to cal-

†Corresponding author. E-mail: wumw@whut.edu.cn

© 2022 Chinese Physical Society and IOP Publishing Ltd

culate the flow field, heat and solute transport. They pointed out that the LBM has great advantages, such as high calculation accuracy, superior convergence, and low computational cost. Likewise, Liu *et al.*[27] used the CA-LBM model to simulate the equiaxed dendritic growth of Al-4.7%Cu alloy and found that the rotation and falling motion significantly affect the dendritic morphology under forced convection. Additionally, Ma *et al.*[28] and Rolchigo *et al.*[29] applied the CA method to the fields of welding and additive manufacturing, and investigated the influence of process parameters on microstructure evolution in molten pool under forced convection by simulation.

Up to date, scholars have carried out plenty of research work on microstructure simulation and many valuable conclusions have been drawn in this period. However, existing studies have not perfectly solved the problem of grid anisotropy in the CA method, thus it is difficult to simulate dendritic growth with random orientations. Meanwhile, for the effect of melt convection on dendritic growth, early simulation studies mainly focused on forced convection. In the actual solidification process, there must be more or less temperature or solute concentration difference in the melt. In this case, natural convection is inevitably formed under the action of gravity, and its influence on the solute distribution and dendritic growth cannot be ignored unless its intensity is much less than that of forced convection.

In this work, a numerical model is developed by coupling the CA method and the LBM to simulate the dendritic growth of metal alloys under convection. An improved decentered square algorithm is embedded into the CA model to eliminate the artificial anisotropy induced by the CA cells. Two- and three-dimensional simulation cases are performed to investigate the effects of both the forced convection and gravity-driven natural convection on the dendritic growth of Al–Cu alloy, based on which the competition growth mechanism of dendrites, the formation of solute plume and interdendritic solute segregation are also discussed.

2. Model description

2.1. Microscopic temperature field

The size unit of the macroscopic grid in the model is mm, but that of the cell in the dendritic growth model is μm. The two orders of magnitude differ greatly. Therefore, the macroscopic data needs to be accurately transmitted to each microscopic cell. In the present work, bilinear interpolation[30] is used to transform the macroscopic temperature data into the microscopic level. Figure 1(a) shows the schematic diagram of the bilinear interpolation method. If the temperature and coordinates of each node in the macroscopic calculation domain are known, the temperature data of the microscopic cell node can be calculated by bilinear interpolation. The calculation method is as follows:

$$\begin{aligned} T(P) = {} & \frac{(x_2-x)(y_2-y)}{(x_2-x_1)(y_2-y_1)}T(Q_{11}) \\ & + \frac{(x-x_1)(y_2-y)}{(x_2-x_1)(y_2-y_1)}T(Q_{21}) \\ & + \frac{(x_2-x)(y-y_1)}{(x_2-x_1)(y_2-y_1)}T(Q_{12}) \\ & + \frac{(x-x_1)(y-y_1)}{(x_2-x_1)(y_2-y_1)}T(Q_{22}), \end{aligned} \tag{1}$$

where $T(P)$ is the node temperature value of a microscopic element, $T(Q)$ is the node temperature value of a macroscopic element, x and y represent the horizontal and vertical coordinates of the node on the macroscopic computing domain, respectively. In the case of three dimensions, select a set of opposite faces, obtain the data of their respective internal nodes through bilinear interpolation, and then interpolate these data again to calculate the temperature value inside the space.

2.2. The lattice Boltzmann method for the fluid flow and solute transport

Compared with the traditional computational fluid dynamics (CFD) calculation methods, LBM has the characteristics of a mesoscopic model between the microscopic molecular dynamics model and macroscopic continuum model. It is widely used to simulate fluid flow and solute transport because of its easy handling of complex boundaries, parallel calculation, and simple programming. Based on the LBM, several models have been developed. Among them, the accuracy of the multi-relaxation-time (MRT) model is higher than that of the single-relaxation-time (SRT) model.[31] However, the MRT-LBM model has high model complexity and low computational efficiency, so the SRT-LBM model is preferred in this work. The SRT-LBM equation can be written as[32]

$$\begin{aligned} & f_i(x+e_i\Delta t, t+\Delta t) - f_i(x,t) \\ = {} & -\frac{1}{\tau}\left[f_i(x,t) - f_i^{\mathrm{eq}}(x,t)\right] + F_i(x,t), \end{aligned} \tag{2}$$

where $f_i(x,t)$ and $f_i^{\mathrm{eq}}(x,t)$ are the particle distribution and equilibrium particle distribution functions, respectively; e_i is the lattice discrete velocity; τ is the relaxation time of the flow field, which is fixed at 1.5 in this work; and Δt is the time step, which can be calculated from the relaxation time τ. The forcing term $F_i(x,t)$ on the right-hand side reads[33]

$$F_i(x,t) = \left(1-\frac{1}{2\tau}\right) w_i \left[\frac{3(\boldsymbol{e}_i-\boldsymbol{u})}{c^2} + \frac{9\boldsymbol{e}_i\cdot\boldsymbol{u}}{c^4}\boldsymbol{e}_i\right]\cdot \boldsymbol{F}\Delta t. \tag{3}$$

According to the Boussinesq approximation, the buoyancy force $\boldsymbol{F}$ due to solute concentration gradient and gravity is expressed as

$$\boldsymbol{F} = -\rho_0 g \beta_C (C - C_0), \tag{4}$$

where $\boldsymbol{g}$ is gravitational acceleration, β_C is solute expansion coefficient, C_0 is the reference solute concentration.

The LBM is similarly applied to the calculation of solute diffusion in the liquid phase region, and its processing method is the same as that of fluid flow calculation. The governing equation of the solute distribution function $g_i(x,t)$ can be written as[34]

$$\begin{aligned} & g_i(x+e_i\Delta t, t+\Delta t) - g_i(x,t) \\ = & -\frac{1}{\tau_{\mathrm{D}}}\left[g_i(x,t) - g_i^{\mathrm{eq}}(x,t)\right] + G_i(xt), \end{aligned} \tag{5}$$

where $g_i^{\mathrm{eq}}(x,t)$ and τ_{D} are the equilibrium distribution function and the relaxation time of the solute concentration field, respectively. The source term $G_i(x,t)$ represents the solute content rejected by the increase in the solid fraction of the interface cell,

$$G_i(x,t) = w_i \Delta f_{\mathrm{s}}(1-k)C, \tag{6}$$

where Δf_{s} is solid fraction increment, k is solute partition coefficient, and C is solute concentration.

The D2Q9 and D3Q15 models are used to simulate two-dimensional and three-dimensional cases, respectively.[35–37] The lattice discrete velocities of the D2Q9 model read

$$[\boldsymbol{e}_i, i=0,\ldots,8] = \begin{bmatrix} 0 & c & 0 & -c & 0 & c & -c & -c & c \\ 0 & 0 & c & 0 & -c & c & c & -c & -c \end{bmatrix}. \tag{7}$$

In the D3Q15 model, the lattice discrete velocities read[38]

$$[\boldsymbol{e}_i, i=0,\ldots,14] = \begin{bmatrix} 0 & c & 0 & -c & 0 & 0 & 0 & c & c & c & c & -c & -c & -c & -c \\ 0 & 0 & c & 0 & -c & 0 & 0 & c & c & -c & -c & c & c & -c & -c \\ 0 & 0 & 0 & 0 & 0 & c & -c & c & -c & -c & c & -c & c & c & -c \end{bmatrix}, \tag{8}$$

where c is the lattice velocity, whose value is the ratio of the space step Δx to the time step Δt. The macro parameters are obtained by the corresponding lattice distribution function:

$$\rho = \sum_{i=0}^{8 \text{ or } 14} f_i, \tag{9}$$

$$\rho \boldsymbol{u} = \sum_{i=0}^{8 \text{ or } 14} f_i \boldsymbol{e}_i, \tag{10}$$

$$C = \sum_{i=0}^{8 \text{ or } 14} g_i, \tag{11}$$

where ρ is fluid density, $\boldsymbol{u}$ is flow velocity. In the two models, the equilibrium distribution functions of the flow field and the solute field are defined as

$$f_i^{\mathrm{eq}}(x,t) = w_i \rho \left[1 + 3\frac{\boldsymbol{e}_i \cdot \boldsymbol{u}}{c^2} + 4.5\frac{(\boldsymbol{e}_i \cdot \boldsymbol{u})^2}{c^4} - 1.5\frac{\boldsymbol{u}^2}{c^2}\right], \tag{12}$$

$$g_i^{\mathrm{eq}}(x,t) = w_i C \left[1 + 3\frac{\boldsymbol{e}_i \cdot \boldsymbol{u}}{c^2} + 4.5\frac{(\boldsymbol{e}_i \cdot \boldsymbol{u})^2}{c^4} - 1.5\frac{\boldsymbol{u}^2}{c^2}\right]. \tag{13}$$

The weight coefficient w_i in the D2Q9 scheme is given as

$$w_i = \begin{cases} 4/9, & i=0, \\ 1/9, & i=1,\ldots,4, \\ 1/36, & i=5,\ldots,8. \end{cases} \tag{14}$$

For the D3Q15 model, w_i is given as

$$w_i = \begin{cases} 2/9, & i=0, \\ 1/9, & i=1,\ldots,6, \\ 1/72, & i=7,\ldots,14. \end{cases} \tag{15}$$

According to the Chapman–Enskog analysis,[34] the relaxation time of flow field τ and solute concentration field τ_D can be calculated by the kinematic viscosity v and solute diffusion coefficient D, respectively,

$$\tau = \frac{3v\Delta t}{\Delta x^2} + \frac{1}{2}, \tag{16}$$

$$\tau_D = \frac{3D\Delta t}{\Delta x^2} + \frac{1}{2}. \tag{17}$$

The unknown particle distribution function on the boundary node needs to be obtained under boundary conditions, so whether the boundary conditions are reasonable has a significant impact on the simulation.[39] In this study, the non-equilibrium extrapolation method is applied to the inlet and outlet boundaries in fluid flow calculation, while the other boundaries are set as periodic boundaries.[40] For the solute field, all boundaries of the computational domain are set as non-diffusion boundaries, and non-equilibrium extrapolation is used in the calculation. Figures 1(b) and 1(c) show the schematic diagrams related to the boundary conditions under forced and natural convection, respectively. In addition, since the melt cannot pass through the dendrites, the solid-liquid interface is considered to be the no-slip and no-diffusion boundary using the bounce-back rule for flow field and solute field simulation.[41]

2.3. The cellular automaton model for dendritic growth

Since simulations on dendritic growth without melt flow based on the CA method were reported in our previous work, the governing equations required for the dendritic growth kinetics are not introduced in this paper. More details can be seen in Ref. [42]. This section focuses on introducing a modified capture rule to simulate dendritic growth with arbitrary orientations.

The growth orientation of dendrites is generally random during metal alloy solidification. However, due to the artificial anisotropy induced by the CA cells, the simulated dendrites usually grow in the orientations of 0° and 45° regardless of the initial orientation value defined in simulations. An improved decentered square algorithm is adopted in this study to eliminate this artificial anisotropy. The decentered square algorithm was first proposed by Rappaz and Gandin,[43] and then modified by Wang *et al.*[44] Recently, Zhu *et al.*[45,46] introduced a geometric factor into the algorithm to ensure the sharp interface of the simulated dendrites. The decentered square algorithm is currently one of the ideal methods for describing the dendritic growth with arbitrary orientation. Figure 1(d) shows the schematic diagram of the decentered square algorithm. When a cell nucleates, its state is transformed from liquid to solid/liquid interface. A father square with the diagonal direction consistent with the crystal orientation is placed in the center. With the dendritic growth driven by the interaction between undercooling and solute diffusion, the solid phase fraction increases, resulting in continuous expansion of the square. When the vertices of the inclined square extend to the surrounding liquid cell, the state of the captured cell is transformed into solid/liquid interface. At the same time, four sub-squares inheriting the growth orientation of the father square are generated with the vertices of the father square as the center. When the solid fraction of the interface cell reaches 1, its state changes to solid, and the corresponding inclined square stops expanding. Additionally, if there are still liquid cells around the solid cell, the liquid cells change to interface cells automatically. The half length of the square diagonal L can be updated as follows:

$$L(t+\Delta t) = L(t) + V_{\mathrm{n}} \cdot \Delta t, \tag{18}$$

where Δt is the time step, V_{n} is the normal velocity of interface cell. Then, the solid fraction is updated by

$$f_{\mathrm{s}} = \frac{L(t+\Delta t)}{\Delta x(|\sin\theta| + \cos\theta)}, \tag{19}$$

where Δx is the cell size, the preferential growth orientation θ is chosen within $-45°$ to $45°$.

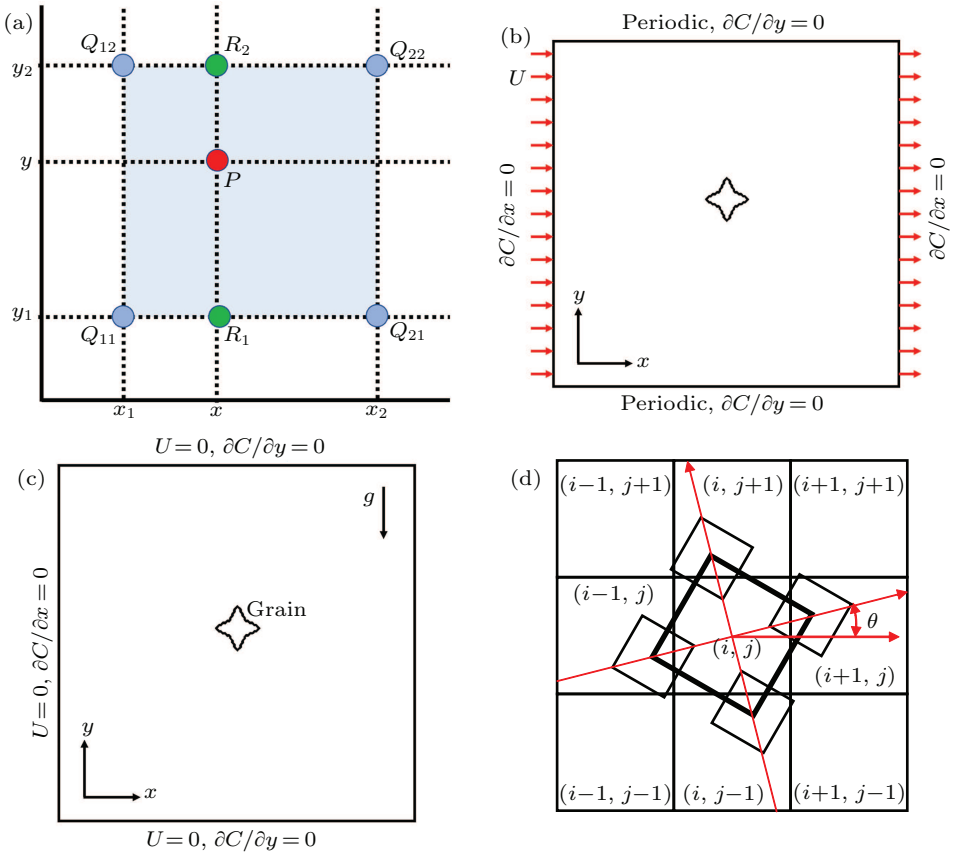


Fig. 1. Schematic diagrams of the issues considered in the model: (a) bilinear interpolation method, (b) boundary conditions under forced convection, (c) boundary conditions under natural convection, (d) decentered square algorithm.

3. Model validation

The Al–Cu alloy is selected in this work, while the physical parameters required for simulation are listed in Table 1. The melt is supposed to be the incompressible Newtonian fluid under convection. In this section, the side length of the square computational domain is 1 mm. A solid seed is planted in the center of the computational domain and its growth orientation is predefined as 0°, 15°, 30° and 45°, respectively. A cool-

ing rate of 60 K/s is set to the melt of the whole calculation domain.

For numerical modeling and simulation, grid density has a great impact on the final results. Refining the mesh improves the accuracy of the results, but drastically reduces the computational efficiency. Therefore, it is crucial to select an appropriate number of grids under the premise of balancing computational efficiency and result accuracy. Figure 2 shows the simulated equiaxed dendritic morphology with different growth orientations under different mesh sizes (1 μm and 2 μm). Comparing the simulation results, we can realize that the scales of the simulated equiaxed dendrites are basically the same, indicating that the algorithm has already effectively eliminated the impact of grid anisotropy and the present numerical model has the capability and stability to simulate dendritic growth with arbitrary orientations. In addition, the mesh size used in this work has a negligible effect on dendrite growth kinetics, but more details of dendrites, such as secondary and higher-order dendritic arms, can be depicted with a finer mesh size.

Table 1. Physical parameters of Al–Cu alloy used in the present study.[47,48]

Definition and unit	Symbol	Value
Initial mass fraction of alloy (wt%)	C	3.00
Liquidus temperature (K)	T_{liq}	922
Liquidus slope (K·wt%$^{-1}$)	m_{l}	−2.6
Solute partition coefficient	k	0.17
Diffusion coefficient in solid (m^2·s^{-1})	D_{s}	3×10^{-12}
Diffusion coefficient in liquid (m^2·s^{-1})	D_{l}	3×10^{-9}
Gibbs-Thomson coefficient (K·m)	Γ	2.4×10^{-7}
Degree of anisotropy of the surface energy	ε	0.027
Density (kg·m^{-3})	ρ	2.475×10^{3}
Viscosity (N·s·m^{-2})	μ	0.014

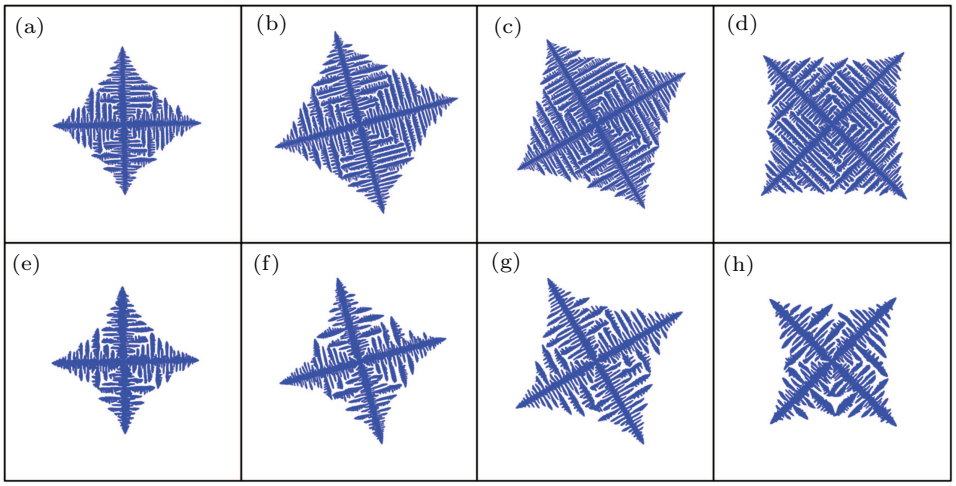


Fig. 2. Simulated equiaxed dendritic morphology with different growth orientations: [(a), (e)] $\theta = 0°$, [(b), (f)] $\theta = 15°$, [(c), (g)] $\theta = 30°$. [(d), (h)] $\theta = 45°$. The upper and lower rows show the equiaxed dendritic morphology with mesh sizes of 1 μm and 2 μm, respectively.

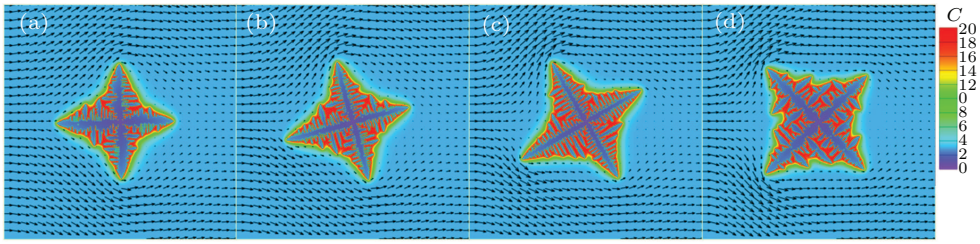


Fig. 3. Simulated equiaxed dendritic morphology with different orientations under forced convection: (a) $\theta = 0°$, (b) $\theta = 15°$, (c) $\theta = 30°$, (d) $\theta = 45°$. The forced convection is constructed in the form of a horizontal melt flow from left to right of the calculation domain with a velocity of 0.4 mm/s.

To verify the feasibility of the established model in simulating dendritic growth under convection, a forced convection is constructed in the form of a horizontal melt flow from left to right of the calculation domain with a velocity of 0.4 mm/s on the basis of the examples in Figs. 2(e)–2(h), and the simulation results are shown in Figs. 3(a)–3(d). It can be seen that the melt flow changes the solute distribution around the equiaxed dendrite, which makes the local undercooling at the dendrite tips different from each other, thereby destroying the symmetry of dendritic morphology. Figure 4 shows the statistical result related to the length of the upstream and downstream primary dendrite trunks under forced convection as indicated in Figs. 3(a)–3(d). The result demonstrates that due to the strong convective transport of solute from the upstream side to the downstream side, the forced convection promotes the growth of dendrite arms at the upstream side and suppresses the growth of downstream dendrite arms. Meanwhile, with the increase of the dendritic orientation angle from 0° to 45°, the four primary dendrite trunks are no longer parallel or perpendicular to the melt flow direction, in the case the

length difference between the upstream and downstream primary dendrite trunks gradually decreases. The laws concluded from the simulation results are in accordance with the reality and previously published works. It is confirmed that the CA-LBM model has the capability of coupling the calculation of temperature field, solute field and flow field.

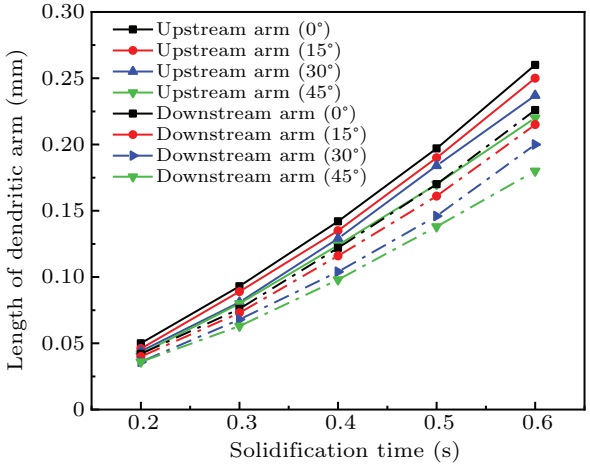


Fig. 4. The length of the upstream and downstream primary dendrite trunks under forced convection with a lateral flow velocity of 0.4 mm s as indicated in Figs. 3(a)–3(d).

4. Simulation results and discussion

4.1. Two-dimensional dendritic growth under forced convection

Simulation cases are performed by the CA-LBM model to study the multiple equiaxed dendritic growths under forced convection. The computational domain is divided into 600×300 square cells with a cell size of 2 μm. To deeply explore the interaction among melt flow, solute distribution and dendritic growth, seeds with random orientation and location are planted in the middle part of the calculation domain, and a lateral melt flow is defined from left to right with a flow velocity of 0.4 mm/s. The cooling rate of the melt in the calculation domain is 60 K/s. Figures 5 and 6 show the simulated multiple equiaxed dendritic growth under forced convection with ten and fifty seeds, respectively.

It can be noted from Figs. 5(a)–5(d) that the melt flows smoothly through the dendrites at the early solidification stage, bringing the solute from the upstream side of each dendrite to the downstream side, so that the development of the primary and secondary dendrite arms is promoted at the upstream side, while their growth is inhibited on the downstream side. As the solidification proceeds, the dendrites on the left grow rapidly under forced convection and hinder the melt flowing to the right. As indicated in Figs. 5(d) and 6(f), the flow velocity in the interdendritic liquid and the right part of the computational domain decreases with the increase of the solid fraction until it approaches zero. In the subsequent stage, the dendrites on the right side grow freely without the action of forced convection. However, the dendrites on the left side are generally still more developed than those on the right side. It can be seen from Fig. 6 that the increase of the seed number makes the interdendritic liquid channels narrower and more complicate. In this case, the blocking effect of dendrites on melt flow is advanced. As shown in Figs. 6(f) and 6(h), the melt flow is already unable to traverse equiaxed dendritic clusters.

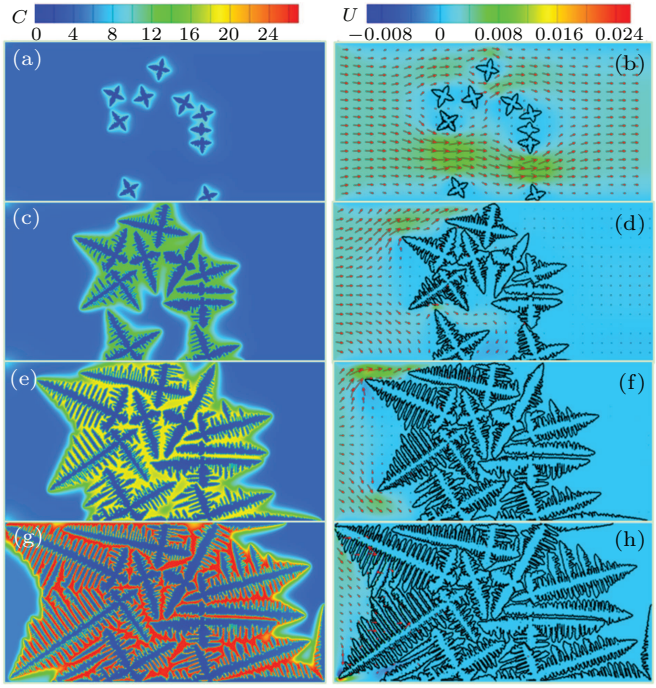


Fig. 5. Simulated multiple equiaxed dendritic growth under forced convection with ten seeds: [(a), (b)] $t = 0.20$ s, [(c), (d)] $t = 0.45$ s, [(e), (f)] $t = 0.70$ s, [(g), (h)] $t = 0.95$ s. The left column shows the solute distribution while the right column shows the flow velocity distribution of the melt.

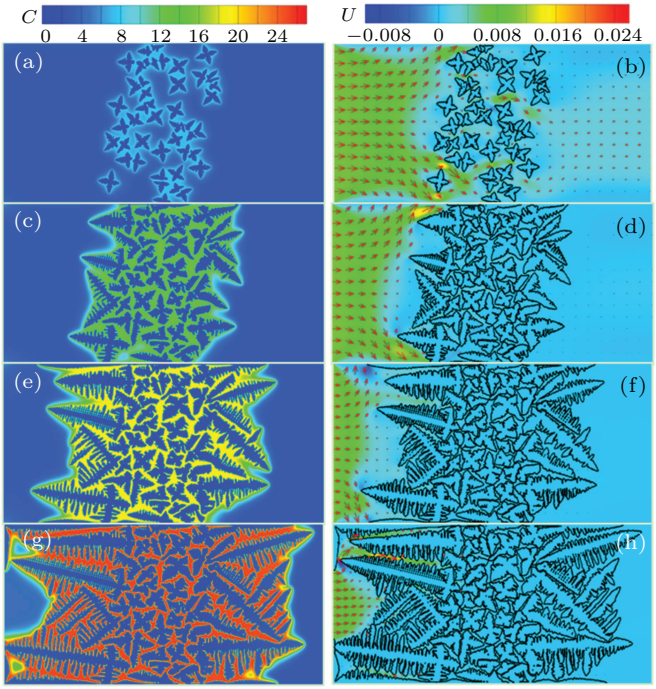


Fig. 6. Simulated multiple equiaxed dendritic growth under forced convection with fifty seeds: [(a), (b)] $t = 0.20$ s, [(c), (d)] $t = 0.45$ s, [(e), (f)] $t = 0.70$ s, [(g), (h)] $t = 0.95$ s. The left column shows the solute distribution while the right column shows the flow velocity distribution of the melt.

According to the simulated results in Figs. 5 and 6, it can be found that the dendritic morphology is quite different at different parts of the calculation domain. The dendrites on the left exhibit a highly asymmetric morphology due to a large space offered on the left side of the calculation domain and the action of forced convection. Competitive growth among these dendrites is related to their growth orientations and forced convection, showing a trend growing towards the upstream side. However, the effect of forced convection on the dendritic growth in the middle part and on the right side of the calculation domain is almost negligible. With the obstruction of dendrites on both sides, the dendrites in the central part show a refined and equiaxed dendritic morphology. Similarly, due to a large space offered on the right side of the calculation domain, the dendrites on the right show an asymmetric morphology with the competitive growth between them.

Figure 7 shows the simulated columnar dendritic growth with and without forced convection. The computational domain is composed of 400×400 square cells with a cell size of 2 μm. Nine seeds with random orientation and location are set at the bottom of the calculation domain. With a temperature gradient of 10 K/mm from bottom to top of the calculation domain, the cooling rate of the melt is 60 K/s. It can be noted from Figs. 7(a)–7(c) that the competitive growth occurs when columnar dendrites with different growth orientations meet with each other, and the columnar dendrites whose growth orientation is more aligned to the heat flow direction always overcome those dendrites with their growth orientations deviating from the heat flow direction. The columnar dendrites with favorable orientations show a strong growth advantage. Side branches appear on the side of the columnar dendrite trunks, and their growth also reflects a competitive growth trend as the same as that of the columnar dendrite trunks. Additionally, the solute is highly accumulated in the interdendritic liquid. Compared to the case under pure diffusion, the presence of forced convection significantly affects the competitive growth between the columnar dendrites. This can be elucidated as shown in Figs. 7(c) and 7(f) taking the dendrites A and B as examples. It can be seen from Fig. 7(f) that the columnar dendrite A with a more favorable growth orientation is blocked by the columnar dendrite B. This is due to the fact that the growth of the columnar dendrite B is promoted under forced convection since its growth direction is more aligned to the upstream side of the melt flow. Consequently, the growth of the columnar dendrite B is dominant and gradually hinders the growth of the columnar dendrite A.

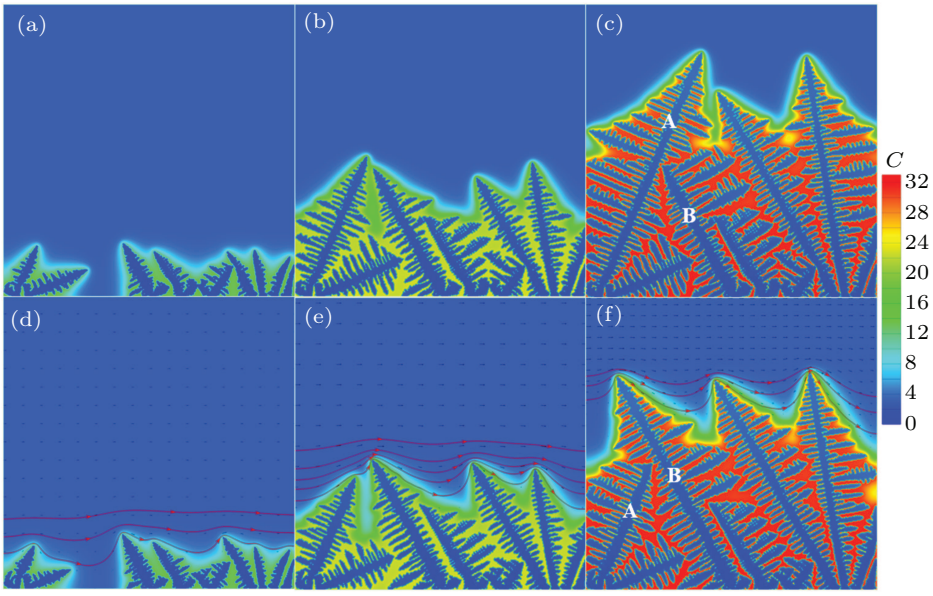


Fig. 7. Simulated columnar dendritic growth under pure diffusion (a)–(c) and forced convection (d)–(f) in the form of a lateral flow with a flow velocity of 0.2 mm/s: [(a), (d)] $t = 0.25$ s, [(b), (e)] $t = 0.6$ s, [(c), (f)] $t = 0.95$ s.

Simulation cases are conducted to further study the overgrowth mechanism of columnar dendrites under pure diffusion and forced convection. The computational domain consists of 400×300 square cells with a cell size of 2 μm. The temperature gradient and cooling rate of the melt are set the same as those in the simulation cases in Fig. 7. Differently, ten seeds are planted at the bottom of the calculation domain with an equal interval, while the first and second halves of the dendrites are named favorably oriented (FO) dendrites and unfavorably oriented (UO) dendrites, respectively according to the heat flow direction. Figure 8 shows the simulated competitive growth of converging columnar dendrites. It can be seen from Figs. 8(a)–8(c) that the FO columnar dendrites always overgrow the UO columnar dendrites during pure diffusion-controlled solidification, which is consistent with the classical dendritic competitive growth theory proposed by Walton and Chalmers.[49] This overgrowth phenomenon usually occurs because of the overlap of the solute fields between the

contacting columnar dendrites. Moreover, the elimination rate of the UO columnar dendrites increases as their growth orientation gradually deviates from the heat flow direction. An unusual competition mechanism appears between converging columnar dendrites with the existence of forced convection. Due to the promotion effect of melt flow on the upstream columnar dendrite arms, the growth of the FO columnar dendrites is hindered by the UO columnar dendrites as shown in Fig. 8(d). As the deviation angle between the growth orientation of the UO columnar dendrites and the heat flow direction increases from 12° to 20° as indicated in Fig. 8(e), the UO columnar dendrites cannot completely block the growth of the FO columnar dendrites. When this deviation angle continuously increases to a specific value such as 30°, the promotion effect of forced convection on the growth of the UO columnar dendrites cannot change their growth weakness, and the growth of those dendrites is inhibited by the FO columnar dendrites as shown in Fig. 8(f). That is to say, the competitive growth of the converging columnar dendrites is determined by the interaction between heat flow and forced convection. The simulated results are in accordance with the conclusions drawn by Jaehoon *et al.*[50] and Pavan *et al.*[51]

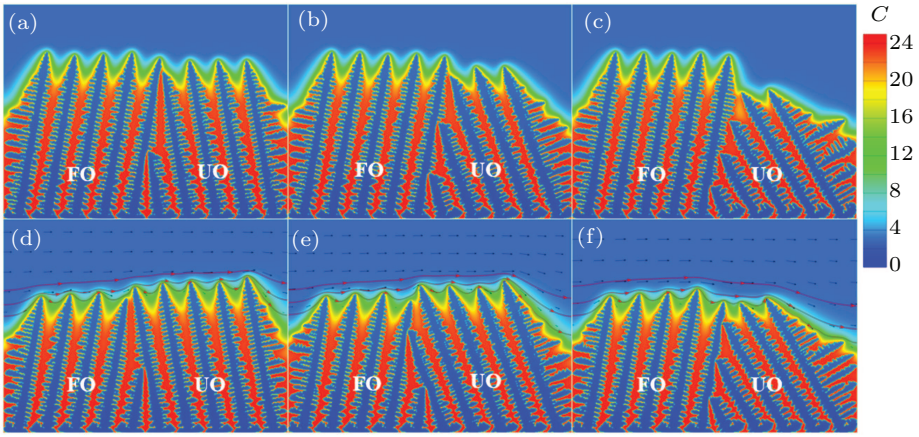


Fig. 8. Simulated competitive growth of converging columnar dendrites under pure diffusion (a)–(c) and forced convection (d)–(f) in the form of a lateral flow with a flow velocity of 0.2 mm/s: [(a), (d)] $\theta_{FO} = 10°$, $\theta_{UO} = 12°$, [(b), (e)] $\theta_{FO} = 10°$, $\theta_{UO} = 20°$, [(c), (f)] $\theta_{FO} = 10°$, $\theta_{UO} = 30°$. Here θ_{FO} and θ_{UO} are the angles between the columnar dendrite trunks and vertical upward direction while they are specified to be positive clockwise.

4.2. Two-dimensional dendritic growth under natural convection

Gravity-driven natural convection is universal in the melt of metal alloys during solidification, especially when there is a significant density difference between the alloying element (solute) and melt, such as the Al–Cu alloy in the present work. Therefore, the CA-LBM model is applied to simulate the dendritic growth of Al–Cu alloy under natural convection. In this section, the computational domain is divided into 400×400 cells with a cell size of 2 μm. A parameter named as the Rayleigh number *(Ra)*, i.e., $Ra = g\beta_C L_0^3 \frac{C_{max}-C_0}{\nu D_l}$, is defined to characterize the intensity of natural convection, where L is the length of the computational domain, C_{max} is the maximum solute concentration. The value of *Ra* is set to be 1×10^7 in this work. Meanwhile, the gravitational direction is vertical downward by default.

Figure 9 shows the equiaxed dendritic growth in the presence of natural convection, while the cooling rate of the melt is 60 K/s in the whole calculation domain. It can be seen that the natural convection induced by the sinking downwards the rejected heavy Cu solute at the solid-liquid interface changes the solute distribution around the dendrite, thereby destroying the four-fold symmetry of the equiaxed dendritic morphology. This is because with the downward sinking of the solute, it accumulates around the dendrite tips at the downstream side. For the Al–Cu alloy, the solute enrichment will lower the liquidus temperature and consequently reduce the local undercooling of the melt. In this case, the growth of primary dendrite trunk at the downstream side is inhibited, while the growth of the upstream primary dendrite trunk is accelerated to a certain extent. As the solidification proceeds, the heavy solute continues to sink downwards, leading to the formation of solute plume in front of the primary dendrite trunk on the downstream side. Under natural convection as marked by the dashed lines with arrows in Figs. 9(b)–9(d), it can be seen that two vortices with opposite rotation directions are formed, which directly have an important influence on the solute distribution.

Except the highly asymmetric growth of the four primary dendrite trunks, the natural convection also leads to dissimilar growth condition of the secondary dendrite arms as indicated in Fig. 9(d). There are well-developed secondary dendrite arms branching on the upward primary dendrite trunk, while the growth of the secondary dendrite arms branching on the upstream side of the two horizontal primary dendrite trunks is severely inhibited due to the enrichment of the heavy solute. Quite unexpectedly, the secondary dendrite arms branching on the downstream side of the two horizontal primary dendrite trunks grow well, and some of them even grow faster than the downward primary dendrite trunk. This can be ascribed to a severe solute enrichment in front of the downward primary

dendrite trunk, while the solute enrichment in front of the secondary dendrite arms is weakened by the two vortices with a strong solute transport capability.

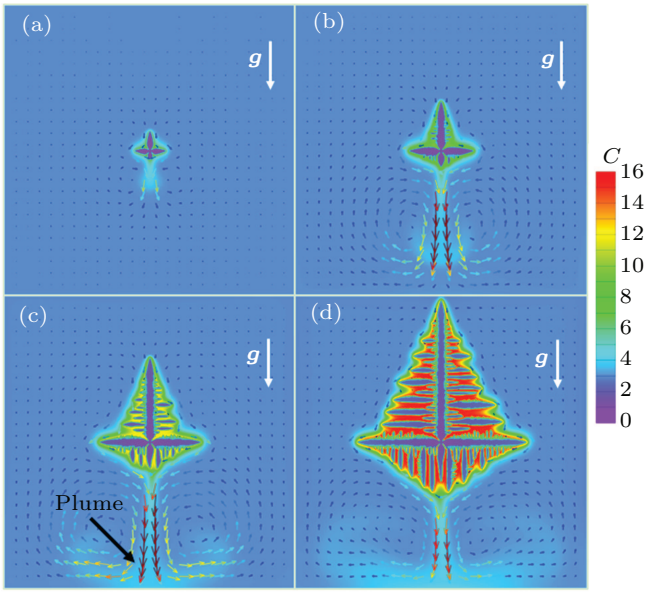


Fig. 9. Simulated equiaxed dendritic growth under natural convection: (a) $t = 0.08$ s, (b) $t = 0.28$ s, (c) $t = 0.48$ s, (d) $t = 0.68$ s.

Compared with the equiaxed dendritic growth, the gravity-driven natural convection may have a greater effect on the growth of columnar dendrites when they grow parallel to the gravity. Figures 10(a) and 10(b) show the simulated columnar dendritic growth under pure diffusion and gravity-driven natural convection, respectively, with a temperature gradient of 10 K/mm from bottom to top of the calculation domain and a cooling rate of 60 K/s in the melt. With the same calculation time, it can be seen from Fig. 10 that the columnar dendrites under natural convection grow faster than those under pure diffusion. This is because the solute accumulation at the dendrite tips is weakened due to the downward sinking of the heavy solute, which is beneficial to the growth of the columnar dendrite tips. With the sinking downwards of the solute, it can be speculated that the degree of solute segregation increases from top to bottom in the liquid regions between the columnar dendrites.

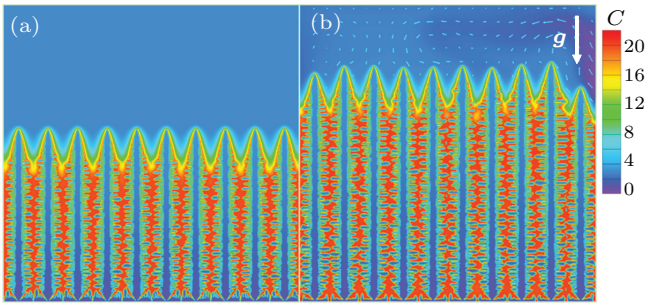


Fig. 10. Simulated columnar dendritic morphology with the same calculation time $t = 0.75$ s: (a) pure diffusion, (b) natural convection. The columnar dendrites grow in the opposite direction of gravity.

Keeping the gravitational direction vertical downward, the same number of seeds as in the simulation cases in Fig. 10 (ten seeds) are planted at the top of the calculation domain. With a cooling rate of 60 K/s in the melt, a temperature gradient of 10 K/mm is set from top to bottom of the calculation domain to ensure that the columnar dendrites grow along the gravitational direction. Figure 11 shows the simulated columnar dendritic growth under natural convection. It can be noted that the rejected heavy solute sinks freely into the liquid phase region, leading to solute accumulation in front of the dendrite tips. With the solute convergence continuously, some solute gradually sinks away from the solute pool and several bulges are formed in front of the solute streams. The expansion of the bulges eventually leads to the formation of chimney-like or mushroom-like solute plumes as illustrated in Fig. 11(c). Compared with the columnar dendritic growth in Fig. 10, it can be seen from Fig. 11 that due to a less solute accumulation in the interdendritic liquid, secondary dendrite arms in the direction of gravity are well-developed, resulting in a decrease of the columnar dendritic arm spacing.

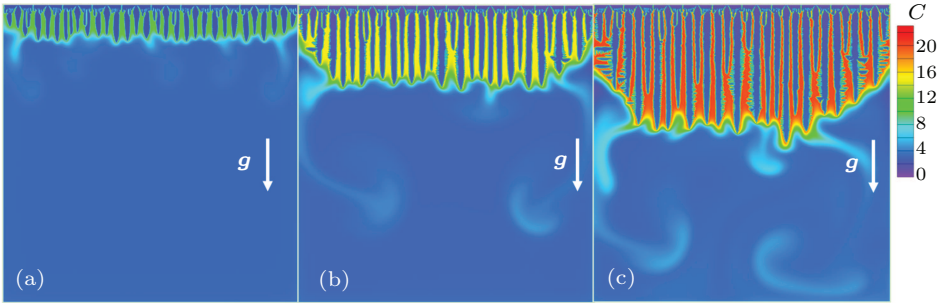


Fig. 11. Simulated columnar dendritic growth under natural convection: (a) $t = 0.25$ s, (b) $t = 0.50$ s, (c) $t = 0.75$ s. The columnar dendrites grow along the gravitational direction.

4.3. Three-dimensional dendritic growth under forced convection

During metal alloy solidification process, the dendrites actually grow in three dimensions, and the melt flow is also in three dimensions. It can be easily expected that the 3D dendritic growth is more complicate than that in the 2D case, and the 3D simulated result of dendritic growth is much closer to the reality. In this section, simulation cases are performed to investigate the 3D dendritic growth of Al–Cu alloy under

forced convection.

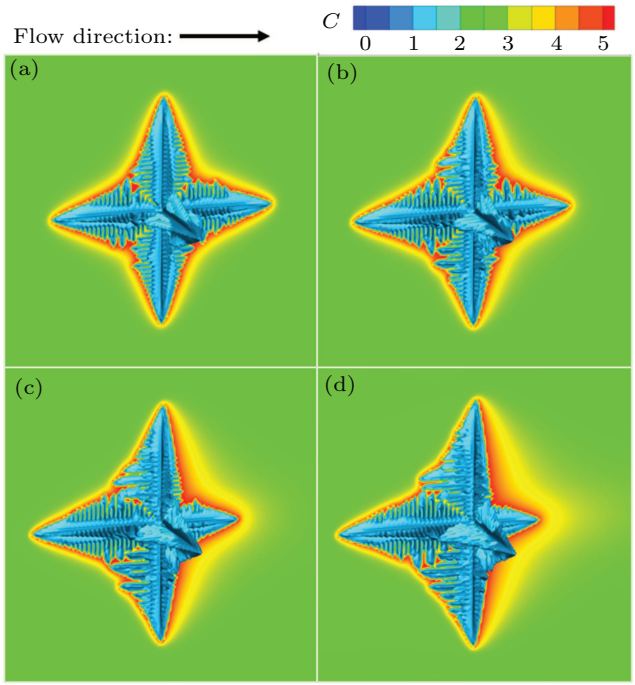


Fig. 12. Three-dimensional equiaxed dendritic growth under forced convection with different inflow velocities: (a) 0 mm/s, (b) 0.15 mm/s, (c) 0.30 mm/s, (d) 0.45 mm/s. The melt flow direction is from left to right of the calculation domain.

For the 3D equiaxed dendritic growth, a solid seed is planted in the middle of the calculation domain consisting of 150×150×150 cubic cells with a cell size of 5 μm. The temperature of the melt in the calculation domain is assumed to be uniform and it cools down from the liquidus temperature at a constant cooling rate of 10 K/s. Figure 12 shows the simulated 3D equiaxed dendritic growth under forced convection with different inflow velocities. It can be seen that the equiaxed dendritic morphology is symmetrical in three dimensions under pure diffusion. However, this symmetrical feature is broken when forced convection is introduced into the calculation procedure. The asymmetric degree increases with a larger inflow velocity. The 3D simulated result is consistent with that in the 2D case as indicated in Fig. 3. Due to the strong convective transport of solute from the upstream side to the downstream side, the forced convection promotes the growth of the primary dendrite trunk at the upstream side and suppresses the growth of downstream primary dendrite trunk. Here, the solute transport effect of the forced convection can be elucidated quantitatively as shown in Fig. 13. Under pure diffusion condition, the solute concentration gradients in front of the dendrite tips on both sides are equal with the same thickness of solute accumulation layer. As the inflow velocity increases, the thickness of the solute accumulation layer in front of the dendrite tip at the upstream side decreases, while it becomes thicker in front of the dendrite tip at the downstream side. As a result, the upstream primary dendrite trunk grows faster than that at the downstream side. It can also be found intuitively from Fig. 12 that with the increase of the inflow velocity, the secondary dendrite arms branching on the two vertical primary dendrite trunks grow well on the upstream side, and they gradually occupy a dominant position in the competition growth with the secondary dendrite arms branching on the horizontal primary dendrite trunk at the upstream side.

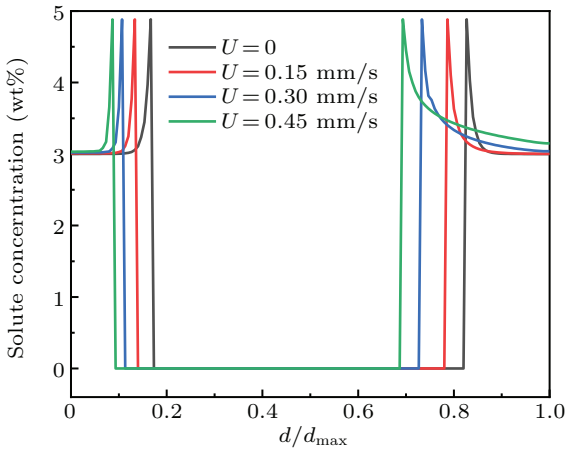


Fig. 13. Solute distribution along the centerline from left to right of the calculation domain as indicated in Fig. 12.

For the 3D columnar dendritic growth, the calculation domain is divided into 150×40×200 cubic cells with a cell size of 5 μm. Three seeds are planted at the bottom of the calculation domain with a uniform interval. With a temperature gradient of 10 K/mm from bottom to top of the calculation domain, the cooling rate of the melt is set to be 10 K/s. Figure 14 shows the simulated 3D columnar dendritic growth with and without forced convection. Under pure diffusion condition, the columnar dendrites grow straightly from bottom to top of the calculation domain, accompanied by solute rejection at the solid-liquid interface. With a similar solute distribution in front of the columnar dendrite tips, the three columnar dendrites grow shoulder to shoulder as shown in Figs. 14(a) and 14(d). When forced convection is introduced, a conspicuous phenomenon can be observed in Figs. 14(b), 14(c) and 14(e), 14(f) that the upstream secondary dendrite arms branching on the three columnar dendrite trunks are more well-developed than those on the downstream side. Meanwhile, the growth of the three columnar dendrites from left to right is gradually accelerated. Here, the liquid region between the left and middle columnar dendrites is defined as region *L*, and the liquid region between the middle and right columnar dendrites is defined as region *R*. It can be noted from Fig. 14(f) that the solute concentration in region *L* is significantly higher than that in region *R*. This can be attributed to the blocking effect of columnar dendrites on melt flow. Since the left columnar dendrite is close to the inlet of melt flow, the intensity of melt flow is relatively strong, bringing the solute at the upstream side to region *L*. However, due to the obstruction of the middle columnar dendrite, the melt flow intensity is weakened to a certain extent. In such a case, the solute in region *L* no longer easily diffuses into region *R*.

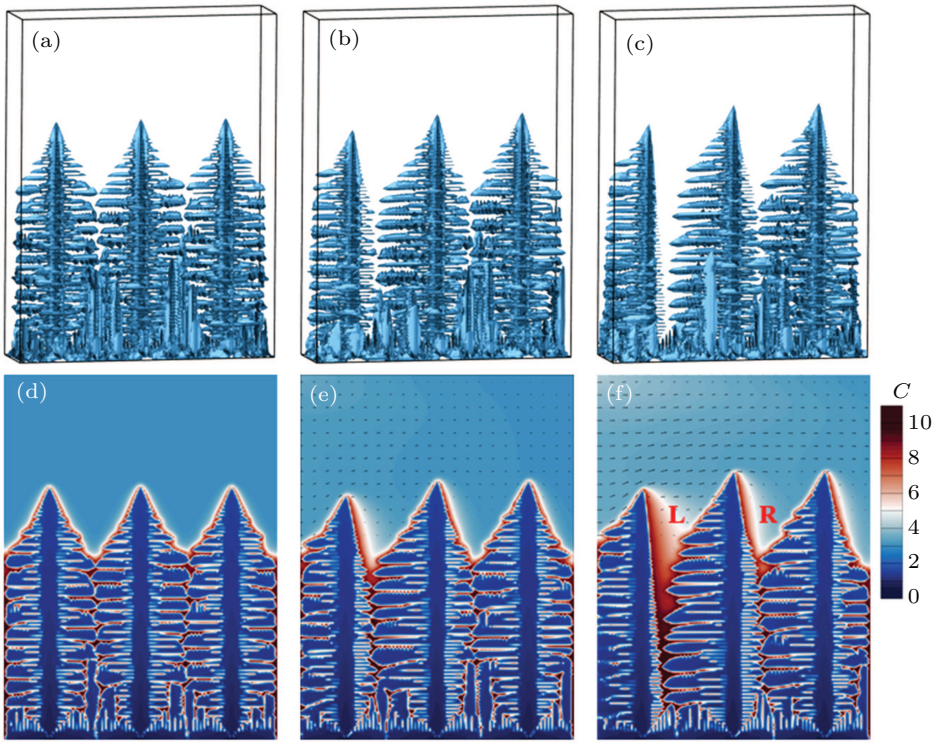


Fig. 14. Three-dimensional columnar dendritic growth under forced convection with different inflow velocities: [(a), (d)] 0 mm/s, [(b), (e)] 0.5 mm/s, [(c), (f)] 1.0 mm/s. The melt flow direction is from left to right of the calculation domain. (a)–(c) The simulated columnar dendritic morphology. (d)–(f) The corresponding solute distribution at the middle cross section parallel to the front view.

5. Conclusions

In this study, a CA-LBM model is developed to simulate the equiaxed and columnar dendritic growth of Al–Cu alloy in both two and three dimensions. The effects of forced and natural convection on the dendritic growth are studied. The following conclusions can be drawn:

(i) By introducing an improved decentered square algorithm into the CA method to eliminate the artificial anisotropy induced by CA cells, the present numerical model has the capability of simulating dendritic growth with arbitrary orientations.

(ii) During multiple equiaxed dendritic growth under forced convection, the increase of solid fraction makes the interdendritic liquid channels narrower and more complicate. The blocking effect of dendrites on melt flow is advanced with a larger number of seeds. The growth of columnar dendrites is promoted when their growth orientation is aligned to the heat flow direction and upstream side of forced convection. The competitive growth of the converging columnar dendrites is determined by the interaction between heat flow and forced convection.

(iii) Gravity-driven natural convection leads to the highly asymmetric growth of equiaxed dendrites. With the sinking downwards of the heavy Cu solute, severe solute segregation forms in the interdendritic liquid when the columnar dendrites grow in the opposite direction of gravity. Conversely, chimney-like or mushroom-like solute plumes are formed in the melt in front of the columnar dendrites when they grow along the gravitational direction.

(iv) The present numerical model has the capability of simulating dendritic growth of Al–Cu alloy under convection in three dimensions. The 3D simulated result is consistent with that in the 2D case. More details on dendritic growth are revealed by 3D simulations.

Acknowledgements

The authors thank Dr. Zhipeng Guo at Tsinghua University (China) and Dr. Ang Zhang at Chongqing University (China) for their helpful discussion.

Project supported by the National Natural Science Foundation of China (Grant No. 51805389), the Key R&D Program of Hubei Province, China (Grant No. 2021BAA048), the 111 Project (Grant No. B17034) and the fund of Hubei Key Laboratory of Advanced Technology for Automotive Components, Wuhan University of Technology (Grant No. XDQCKF2021011).

References

[1] Tang Y, Wu Y, Zhang Y, Dai Y B, Dong Q, Han Y F, Zhu G L, Zhang J, Fu Y N and Sun B D 2021 *Acta Mater.* **212** 116861

[2] Ren N, Li J, Panwisawas C, Xia M X, Dong H B and Li J G 2021 *Acta Mater.* **206** 116620

[3] Wang T, Hachani L, Fautrelle Y, Delannoy Y, Wang E, Wang X D and Budenkova O 2020 *Int. J. Heat Mass Transfer* **151** 119414

[4] Qin L, Shen J, Li Q D and Shang Z 2017 *J. Cryst. Growth* **466** 45

[5] Hachani L, Zaidat K and Fautrelle Y 2015 *Int. J. Heat Mass Transfer* **85** 438

[6] Peng P, Li S Y, Zheng W C, Lu L and Zhou S D 2021 *Trans. Nonferrous Met. Soc. China* **31** 3096
[7] Ngomesse F, Reinhart G, Soltani H, Zimmermann G, Browne D J, Sillekens W and Nguyen-Thi H 2021 *Acta Mater.* **221** 117401
[8] Shevchenko N, Boden S, Gerbeth G and Eckert S 2013 *Metall. Mater. Trans. A* **44** 3797
[9] Shevchenko N, Roshchupkina O, Sokolova O and Eckert S 2015 *J. Cryst. Growth* **417** 1
[10] Akamatsu S and Henri N T 2016 *Acta Mater.* **108** 325
[11] Henri N T, Luc S, Ragnvald H M, Lars A, Bernard B, Michel S and Guillaume R 2012 *C. R. Phys.* **13** 237
[12] Clarke A J, Tourret D, Song Y, Imhoff S D, Gibbs P J, Gibbs J W, Fezzaa K and Karma A 2017 *Acta Mater.* **129** 203
[13] Yan X W, Xu Q Y and Liu B C 2017 *J. Cryst. Growth* **479** 22
[14] Gu C, Ridgeway C D, Moodiispaw M P and Luo A A 2020 *J. Mater. Process. Technol.* **286** 116829
[15] Xiong L D, Zhu G L, Mi G Y, Wang C M and Jiang P 2021 *J. Alloy. Compd.* **858** 157669
[16] Takaki T, Sato R, Rojas R, Ohno M and Shibuta Y 2018 *Comput. Mater. Sci.* **147** 124
[17] Ratkai L, Pusztai T A and Granasy L 2019 *npj Comput. Mater.* **5** 1
[18] Zhang Q Y, Sun D K, Zhang S H, Wang H and Zhu M F 2020 *Chin. Phys. B* **29** 078104
[19] Rodgers T M, Moser D, Abdeljawad F, Underwood Jackson O D, Carroll J D, Jared B H, Bolintineanu D S, Mitchell J A and Madison J D 2021 *Addit. Manufact.* **41** 101953
[20] Zhang Z D, Cao Y T, Sun D K, Xing H, Wang J C and Ni Z H 2020 *Chin. Phys. B* **29** 028103
[21] Song Y H, Wang M T, Ni J, Jin J F and Zong Y P 2020 *Chin. Phys. B* **29** 128201
[22] Song W, Zhang J M, Wang S X, Wang B and Han L L 2016 *J. Cent. South Univ.* **23** 2156
[23] Fang H, Xue H, Tang Q Y, Zhang Q Y, Pan S Y and Zhu M F 2019 *Acta Phys. Sin.* **68** 048102 (in Chinese)
[24] Zhu M F, Dai T, Lee S Y and Hong C P 2008 *Comput. Math. Appl.* **55** 1620
[25] Sun D K, Chai Z H, Li Q and Lin G 2018 *Chin. Phys. B* **27** 088105
[26] Yin H, Felicelli S D and Wang L 2011 *Acta Mater.* **59** 3124
[27] Liu L, Pian S, Zhang Z, Bao Y, Li R and Chen H 2018 *Comput. Mater. Sci.* **146** 9
[28] Ma R, Dong Z B and Wei Y H 2009 *Cryst. Res. Technol.* **44** 1197
[29] Rolchigo M R, Mendoza M Y, Samimi P, Brice D A, Martin B, Collins P C and Lesar R 2017 *Metall. Mater. Trans.* **48** 3606
[30] Daud A and Bilal M 2014 *Appl. Math. Comput.* **233** 72
[31] Chai Z H and Shi B C 2020 *Phys. Rev. E* **102** 023306
[32] Qian Y H, Humieres D D and Lallemand P 1992 *Europhys. Lett.* **17** 479
[33] Guo Z L, Zheng C G and Shi B C 2002 *Phys. Rev. E* **65** 046308
[34] Shi B C, Deng B and Chen X W 2007 *Comput. Math. Appl.* **55** 1568
[35] Zhang L Q, Yang S L, Zeng Z and Chew J W 2018 *Comput. Fluids* **176** 153
[36] Riheb M, Hassane N, Hacen D, Sihem H and Zohir Y 2020 *Int. Commun. Heat Mass Transfer* **119** 104992
[37] He S Y, Habte B T and Jiang F M 2017 *Int. Commun. Heat Mass Transfer* **82** 1
[38] Mei R W, Shy Y W, Yu D Z and Luo L S 2000 *J. Comput. Phys.* **161** 680
[39] Leila J, Nor A C S, Alireza F and Mahmoud P H A 2016 *Int. Commun. Heat Mass Transfer* **78** 1
[40] Guo Z L, Zheng C G and Shi B C 2002 *Chin. Phys.* **11** 366
[41] Paul L, Pierre B J and Alain N 1991 *Physica D* **47** 233
[42] Wu M W and Xiong S M 2012 *Trans. Nonferrous Met. Soc. China* **22** 2212
[43] Gandin C A and Rappaz M 1994 *Acta Mater.* **42** 2233
[44] Wang W, Lee P H and Mclean M 2003 *Acta Mater.* **51** 2971
[45] Zhu M Y, Wang W L, Ji C and Luo S 2018 *Metall. Mater. Trans.* **49** 200
[46] Zhu M Y, Gao X H, Meng X N, Cui L, Zhang K and Meng Y F 2020 *Mater. Res. Express* **7** 056505
[47] Zhang Q Y, Sun D K, Pan S Y and Zhu M F 2020 *Int. J. Heat Mass Transfer* **146** 118838
[48] Sun D K, Zhang Q Y, Cao W S and Zhu M F 2015 *Chin. Phys. Lett.* **32** 68103
[49] Walton D and Chalmers B 1959 *Trans. Metall. Soc. AIME* **215** 447
[50] Jaehoon L, Ohno M, Shibuta Y and Takaki T 2021 *J. Cryst. Growth* **558** 126014
[51] Pavan L V, Wang F, Michael S and Britta N 2021 *Comput. Mater. Sci.* **186** 109964